Experimental Investigation of Pilot-Fuel Combustion in Dual-Fuel Engines, Part 2: Understanding the Underlying Mechanisms by means of Optical Diagnostics Highlights

Aleš Srna, Beat von Rotz, Michele Bolla, Yuri M Wright, Kai Herrmann, Konstantinos Boulouchos, Gilles Bruneaux

Title:

Experimental Investigation of Pilot-Fuel Combustion in Dual-Fuel Engines, Part 2: Understanding the Underlying Mechanisms by means of Optical Diagnostics

Authors:

Aleš Srna*[1], Beat von Rotz[1], Michele Bolla[2], Yuri M. Wright[2,3], Kai Herrmann[4], Konstantinos Boulouchos[2], Gilles Bruneaux[5]

1. Paul Scherrer Institute, Energy and Environment Division, Forschungstrasse 111, CH-5232 Villigen PSI, Switzerland
2. ETH Zürich, Institute for Energy Technology, Laboratory for Aerothermochemistry and Combustion Systems, Sonneggstrasse 3, CH-8092 Zürich, Switzerland
3. Combustion & Flow Solutions GmbH, Switzerland
4. University of Applied Sciences Northwestern Switzerland, Institute of Thermal and Fluid Engineering, School of Engineering, Klosterzelgstrasse 2, CH-5210 Windisch, Switzerland
5. IFP Energies nouvelles, 1 et 4 avenue de Bois Préau, 92852 Rueil-Malmaison, France; Institut Carnot IFPEN Transports Energie

*Corresponding author (A. Srna): ales.srna@psi.ch

Abstract

The pilot-fuel auto-ignition and combustion under engine like conditions in compressed methane/air mixtures have been investigated. Experiments were performed in an optically accessible Rapid Compression-Expansion Machine featuring quiescent charge conditions and a single-hole coaxial diesel injector mounted on the cylinder periphery. In Part 1, the phenomenology of the pilot-fuel combustion has been studied based on the thermodynamic analysis. With the addition of methane, a strongly prolonged pilot-fuel combustion duration was observed, especially at increased EGR rates. The aim of Part 2 is to improve the understanding of the underlying processes governing the pilot-fuel burning and premixed flame initiation in dual-fuel engines. For this purpose, the thermodynamic analysis was supplemented by the application of optical diagnostics including high-speed CH_2O-PLIF, Schlieren and OH* chemiluminescence, and corroborated with homogeneous reactor and laminar flame speed calculations. The investigations focused on determining the role of (a) ignition location and number of ignition kernels, (b) stratification of the ignition delay due to the chemical influence of methane and (c) the role of flame propagation during the pilot-fuel burning. In the initial phase, the combustion was found to propagate through an auto-igniting front. When combustion reaches the lean zones with high ignition delay spatial stratification, the premixed flame propagation becomes the dominant mechanism owing to its higher spreading rate. Both processes influence the pilot-fuel combustion duration. With increasing methane concentration the simulations predict increasing stratification of the ignition delay in lean regions, and a moderately increased laminar flame speed in the pilot-fuel lean regions. Overall, this explains the observed trends of longer pilot-fuel burning in the dual-fuel cases and indicates an increasing role of flame-propagation in the dual-fuel combustion pilot-fuel burning.

Keywords:

Dual-fuel combustion; natural-gas engines; combustion mode transition; autoignition; high-speed CH_2O-PLIF; optical diagnostics;

Highlights:

- Ignition occurs in the fuel-richest regions within the pilot-fuel jet
- Chemical influence of methane on the transition from ignition to premixed flame
- Competing processes of auto-ignition front and flame propagation
- Increased role of the flame propagation in the dual-fuel combustion at EGR cases

1 Introduction

Lean-premixed pilot-fuel ignited natural gas engines are seen as an attractive solution to fulfill the present and future emission legislation at uncompromised efficiency and lower fuel specific CO_2 emissions. Despite the proven benefits at medium and high loads, a clear emissions/efficiency tradeoff has been demonstrated at low loads – large pilot-fuel portions lead to high emissions of soot and NO_x while reducing the pilot-fuel portion yields to a penalty in engine efficiency and high unburnt hydrocarbons emissions (UHC) [1-6]. Usually, dual-fuel engines are engineered by modifications of their diesel/gasoline counterparts. Therefore, it can be assumed that by further development of their engine geometry as well as control systems considerable improvements in efficiency and emission levels can be achieved. This unused potential has motivated several engine experiments and optical investigations with regard to dual-fuel combustion, e.g. [2, 4-12].

Generally, it is understood that methane has a strong inhibiting effect on the pilot-fuel autoignition. With the addition of methane into the air charge at otherwise unchanged conditions, prolonged ignition delays have been observed for several technical and surrogate fuels [9, 10, 13-15]. A recent study by the authors [14] has revealed that this influence originates from methane reducing pilot-fuel reactivity during the first-stage pilot-fuel autoignition, leading to a delayed onset of the first-stage ignition in lean pilot-fuel regions. Through the turbulence-chemistry interaction, this influence is propagated to the fuel-rich regions and leads to a delayed high-temperature ignition [14, 16]. This interaction can ultimately lead to misfire as well as adverse effects on cyclic variability, engine efficiency, and UHC emissions [2, 4, 7, 17-19].

While investigations on the influence of methane on ignition are established in the literature and understood to a certain extent, considerably fewer studies have been performed with regard to the impact of methane during the transition phase into premixed flame propagation. In this time, the pilot-fuel is being consumed during high-temperature reactions while the in-cylinder flow-field is still dominated by momentum induced by the pilot spray. However, the conventional engine test-rigs feature very turbulent charge conditions and therefore, the rapid premixed flame propagation masks the pilot-fuel heat release rate (HRR) [20], making assumptions on the pilot-fuel burning period challenging. Usually, lower pressure rise rates and longer combustion duration were observed in dual-fuel operation relative to the equivalent diesel mode [3]. Nevertheless, to track the in-cylinder consumption of the pilot-fuel under such turbulent conditions would require a highly-advanced set of optical diagnostics. To the authors' best knowledge no such studies have been reported in the literature.

The pilot-fuel burning phase has a paramount influence on the combustion of the premixed fuel. The timing, size, and evolution of the initiated flame kernels strongly influence the flame front evolution and were shown to influence the UHC emissions as well as efficiency [4, 17-19, 21]. Generally, the process is understood as a competition between an auto-igniting flame-front and premixed flame propagation [22-24]. Also in other combustion concepts like RCCI and partially premixed combustion studies the pilot-fuel injection strategy was shown to be the main parameter governing the engine efficiency and HRR [25-27]. At low injection pressures, conical flame kernels were observed, while higher injection pressures lead to a toroidal flame front [11]. Both the 0D/1D as well as CFD models have to be able to reproduce such characteristics for accurate HRR predictions. Many dual-fuel CFD models switch between an auto-ignition and a flame-propagation model, using different approaches to distinguish when a premixed flame has been established and to switch the model accordingly [24]. Also, the 0D-models rely on different assumptions when to change the HRR prediction model, for example by assuming conical ignition kernels and the pilot-fuel combustion duration to be proportional to the ignition delay [20].

This study aims to shed light on the underlying processes governing the transition from pilot-fuel ignition to premixed flame propagation in dual-fuel engines. An optically accessible RCEM featuring quiescent conditions was used. In Part 1 of this work, the first-order influences of the charge and pilot-injection parameters on the pilot-fuel burning phase were identified based on HRR analysis. Premixed methane was found to increase the pilot-fuel combustion duration, but nevertheless, strongly decoupled from the ignition delay under some conditions. In Part 2, we corroborate these findings with high-fidelity optical diagnostics to (a) improve the understanding of the underlying fundamental processes of the combustion and (b) to confirm the conclusions of the HRR analysis. In particular, the interaction between the following processes/effects with regard to the transition time have been investigated: (a) the extent of autoignition front governing the pilot-fuel combustion, (b) the role of flame propagation during the pilot-fuel burning, and (c) the contribution of the number and distribution of the ignition kernels. High-speed CH_2O-PLIF at 10 kHz was used to trace the persistence of pilot-fuel cool-flame combustion products, complemented by high-speed Schlieren and OH* chemiluminescence imaging at a higher frame rate (80 and 40 kHz, respectively) to trace the appearance of ignition kernels and the spreading rate of the burnt zones.

The publication is structured as follows: First, the optical diagnostic setup is introduced. The results section presents the pilot-fuel combustion single-event visualizations in diesel and dual-fuel cases for a variation of pilot-injection strategy. Both CH_2O-PLIF and OH* chemiluminescence results are presented. The evaluation of these results is supported by homogeneous reactor and laminar flame-speed calculations in order to investigate the methane influence on the propagation speeds of the competing combustion modes. Through the discussion, the conclusions on the importance of the governing processes during the pilot-fuel burning in dual-fuel engines are drawn.

2 Experimental setup

The experimental setup used in Part 2 of this study is the same as described in detail in Part 1 and the references within. Therefore, only a summary is offered here. Experiments were performed in an optically accessible Rapid Compression Expansion Machine (RCEM) with a bore of 84 mm and BDC displacement of 1.38 dm^3 (249 mm stroke clearance). Pilot-fuel has been admitted into a compressed methane/air mixture using a side-mounted 100 µm single-hole coaxial diesel injector. Charge conditions in the RCEM are quiescent throughout the cycle. Optical access into the RCEM combustion chamber is offered through two Ø52 mm windows along the cylinder axis as well as through the Ø36 mm side-window used for illumination with a laser-sheet.

Experiments were performed at a pressure at the Start of Injection (SOI) of 25 bar. Experimental matrix includes variation of temperature at the SOI (T_{SOI}, 770 – 850 K), methane equivalence ratio (ϕ_{CH4}, range 0 – 0.66), charge oxygen content ($[O_2]$) as well as a variation of pilot injector energizing time (ET, 300 – 500 µs) and injection pressure (p_{inj}, 600 – 1000 bar). In Part 1, we were focusing on the combustion heat release rate (HRR) analysis complemented with non-reactive quantitative optical investigations of pilot-fuel mixing by application of tracer-PLIF, Schlieren, and Mie-scattering. In Part 2, the HRR analysis is complemented with optical imaging of CH_2O (CH_2O-PLIF), Schlieren and OH* chemiluminescence imaging under reactive conditions.

2.1 CH_2O-PLIF, Schlieren and OH chemiluminescence optical setup*

Simultaneous high-speed imaging of CH_2O-PLIF, Schlieren, and hydroxyl chemiluminescence (OH*) has been employed along the same optical axis to simultaneously temporally resolve the consumption of low-temperature combustion products (CH_2O-PLIF) as well as to detect the high-temperature ignition and flame-kernels spreading (Schlieren and OH*). The optical arrangement at the RCEM is shown in Figure 1.

A Schlieren beam passed the combustion chamber along the injector axis. The same Schlieren setup and settings as used for the non-reactive measurements (Part 1) was used here as well. Schlieren imaging frame-rate was 80 kHz. Dichroic mirrors were used to separate the short-wavelength CH_2O-PLIF and OH* signal from the Schlieren beam, therefore, enabling imaging with the three methods along the same optical axis. All devices were synchronized to the electronic start of injection trigger using a LaVision timing unit.

2.1.1 CH_2O-PLIF

The formaldehyde fluorescence has been excited using a 3rd harmonic output of a high-speed diode-pumped Q-switched Nd:YAG laser (Edgewave IS400, 7.5 mJ/pulse at 355 nm, 10 kHz repetition rate). A laser sheet with a height of 50 mm and about 1 mm thickness has been formed using a combination of cylindrical and spherical lenses. The central 32 mm of the laser-sheet were directed towards the injector orifice under an angle of 3.5° relative to the plane of the cylinder head surface. On the detection side, the radiation in the wavelength range of 350 – 500 nm has been separated from the Schlieren beam with a dichroic beamsplitter plate (Newport 66238). The bandpass filtered PLIF signal (400 – 480 nm, Chroma technology) was collected with a Nikkor 105mm f/2.8 glass lens and detected with an image intensifier (LaVision HS-IRO) coupled to a high-speed camera (Photron Fastcam SA1.1). The projected pixel size was 0.11 mm/pixel. Intensifier gate was set to 100 ns, and the gain setting was 37 counts/photoelectron. Image flat-field correction has been performed by the tracer-PLIF images of homogeneously seeded TMPD vapor in a nitrogen atmosphere which was introduced into the combustion chamber of the RCEM. The pulse energy fluctuations were corrected by measuring the intensity of the sampled laser beam using a fast photodiode and SRS Boxcar integrator.

During the auto-ignition process, the moving piston compresses the fuel cloud towards the cylinder head. This motivates the 3.5° angle of the laser-sheet plane instead of the plane along the injector axis (5° inclination). In a pre-study, two high-speed intensified cameras detecting OH* chemiluminescence simultaneously through the main and the side window have been used to determine the axial and radial position of the ignition spot. This optimal laser-sheet inclination of 3.5° has been selected based on a best-fit through the ignition spots under different conditions.

The detection of CH_2O by 355 nm-PLIF excitation in sooting diesel sprays is known to suffer from interference by polyaromatic hydrocarbons (PAH) [28, 29] and laser-induced incandescence (LII) [30]. Only a small portion of the investigated conditions in this study were under sooting conditions [31]. In this cases, the PAH interference was distinguished from CH_2O-PLIF based on the differences in the relative intensity [32] and the spatial and temporal criterion [29, 30, 33].

2.1.2 OH* chemiluminescence

Filtered flame emission in the spectral range of chemically excited hydroxyl (OH*) has been acquired using a second intensified high-speed camera (Photron FastCam SA1.1 with LaVision HS-IRO) at a frame rate of 40 kHz. The intensifier was equipped with an UV lens (Sodern Cerco 100 mm f/2.8) and bandpass filter (313 nm +/- 13 nm). The resulting resolution was 0.18 mm/pixel. Intensifier gate was set to 20 us, and the gain was adapted to the brightness of the flame emission under different conditions (9-45 counts/photoelectron). A higher intensifier gain was necessary under reduced [O_2] cases due to the significant decrease in OH* emission. The gain setting of up to 190 counts/photoelectron was used to achieve best-possible signal-to-noise ratio. The UV radiation has been separated from the Schlieren beam using a 308 nm 45° laser mirror (100 mm diameter).

2.2 Imaging results and processing

An exemplary image-series of a dual-fuel combustion event is presented in Figure 2. Images from all three optical methods are presented down-sampled to the 10 kHz frame-rate of CH_2O-PLIF imaging. Schlieren-images show a typical two-stage ignition event – first, a contrast-decrease of the Schlieren-contours has been detected at the spray periphery as the first CH_2O-PLIF signal appears at 0.84 ms aSOI. The low-T reactivity then spreads along the spray periphery towards the spray tip and towards the spray axis. At the same time the Schlieren contrast further reduces, and just before ignition (1.24 ms) barely any Schlieren signal is visible. This disappearance of the Schlieren signal is attributed to the heat-release from the first-stage ignition compensating for the refractive index change due to the fuel evaporative cooling and has been reported before for both diesel [29, 34] and dual-fuel combustion [9, 35]. Ignition occurs between the image panels at 1.24 and 1.34 ms and is indicated by the disappearance of a part of the CH_2O-PLIF cloud, the reappearance of the Schlieren signal with high contrast, and the first appearance of the OH* chemiluminescence signal. Ignition kernel then spreads through the pilot-fuel cloud, and the remaining CH_2O is quickly consumed except close to the injector orifice. At the same time, the Schlieren contour spreads and smoothens as the laminar flame propagation is initiated. A very high rise of the OH* signal is observed at the same time.

Analysis of the HRR (Figure 2, bottom plot) shows good agreement of the cool-flame and high-temperature peaks of the HRR to the interpretation of the optical results. The source of the moderate-intensity signal in CH_2O-PLIF images at late-times after ignition (wide-spread, covering the center of the burnt area) has been attributed to strong CO_2* fluorescence based on the spectrally resolved flame-emission detection (not shown) using a similar diagnostic setup as [36].

The optical data was further processed to extract the spray and flame contours as well as to detect the ignition and flame-kernels. Schlieren images were processed using the adaptive background subtraction methodology as proposed by the Engine Combustion Network [37]. The processing begins with the first acquired image serving as the background, subtracted from the following image. After background subtraction, the spray/flame regions are separated from the surrounding based on a thresholding approach, and the process continues with assuming the regions without any spray detected as the new background, whereas the previous background is assumed for the regions with spray detected. This adapted background is then subtracted from the next image. The threshold was selected in a trial-and-fail procedure until the methodology reliably detected the spray-contour. The quality of this approach is demonstrated by the red/black contours in Figure 2. The automated spray-contour detection just prior to ignition is not reliable and not drawn due to the strongly diminished Schlieren signal.

Also, the OH* chemiluminescence images were processed using a thresholding approach. Ignition was detected by the OH* signal exceeding a threshold of 40 counts in an area larger than 60 pixel. This threshold related to the lowest intensifier gain and was selected as the minimal threshold reliably separating ignition cores from the noise. This threshold level was adapted analogously to the higher intensifier gain setting. The thresholding method is also proposed by the Engine Combustion Network [37] and found to very reliably detect the ignition. Nevertheless, in the reduced charge [O_2] cases a lower threshold (20 counts) with manual checking was necessary to avoid over-predicted ignition delay due to the considerably reduced OH* signal.

A thresholding technique was also used to determine the evolution of the flame-kernels. Nevertheless, the strong scattering of light from the bright central burnt zones was found to raise the signal level over the entire window to a higher level than the background before ignition. Therefore, after ignition was detected, the threshold for flame spreading has been adapted based on the highest flame brightness in each frame – 40 counts plus 2% of the maximal detected brightness.

3 Results

The results section first establishes the theoretical background for combustion transition process by simulating the influence of methane on the auto-ignition front and premixed flame spreading rate. Homogeneous reactor (HR) and laminar flame speed calculations are presented for this purpose. These calculations, despite representing a very simplified view of the transition process, yielded consistent predictions of methane influence on the transition process. In the second part, the experimental evidence for the calculated influences is fathomed by comparing the pilot-fuel consumption and flame spreading of the diesel and dual-fuel combustion events.

3.1 Calculations: Methane influence on the auto-ignition front and laminar flame spreading rates

The spreading rate of an auto-ignition flame front can be described by the Zeldovich criterion as the inverse of the gradient of auto-ignition time. In pilot-fuel jets, the auto-ignition time stratification correlates in the first-order to the mixture spatial stratification, if neglecting the mixing history of different fuel parcels and the turbulence-chemistry interactions [14, 38]. To estimate the effect of methane on the autoignition time stratification in the mixture space, homogeneous reactor calculations were employed, using the reduced chemical mechanism by Ranzi et al. (130 species, 2323 reactions, [39]). This mechanism choice was motivated by the findings of a comprehensive mechanism assessment for methane/dodecane air mixtures reported in [40]. Additionally, the calculations were repeated for a subset of cases using the substantially more complex detailed mechanisms (Polimi [41] and LLNL [42]) yielding

qualitatively the same conclusions. The 80% temperature rise criterion, as proposed in [38], was applied to detect the ignition. Figure 3a shows the high-temperature ignition delay from HR calculations at T_{SOI} = 770 K for different ϕ_{CH4}.

Addition of methane shifts the most reactive mixture towards richer pilot fuel conditions and delays the ignition by about 20%. At fuel-richer mixture fractions, the influence of methane diminishes. On the other hand, a considerable stratification of the ignition delay is observed in the pilot-lean regions especially when leaner than $\phi_{CH4} = 0.5$. In addition, to highlight the methane role in the chemical reactions, the dotted line in Figure 3a shows the calculation for $\phi_{CH4} = 0.66$ with methane initiated as an inert species – not participating in the chemical reactions but diluting the mixture and changing its thermal capacity (as proposed in [9] and [14]). An about four-times lower ϕ_{CH4} influence was predicted with inert methane species, indicating a strong chemical involvement of methane in the lean-mixtures autoignition.

The auto-ignition time gradients in the lean-mixtures considerably increase with the introduction of methane. For example, already at $\phi_{C12} = 0.45$ a 45% increase of the ignition delay is predicted. In absolute terms, this increase is three-times higher than the increase of ID in the most reactive mixtures. Therefore, the Zeldovich criterion [43] will predict a considerable increase of the propagation time across the mixture, especially in the cases when very lean pilot-fuel mixtures at ignition are achieved. This is in agreement with the prolonged pilot-fuel combustion duration reported in Part 1 of this study.

Figure 3 b) and c) additionally assess the methane influence on ignition for a variation of T_{SOI} (b) and variation of $[O_2]$ (c). Only the $\phi_{CH4} = 0$ and 0.66 curves are plotted for clarity. Under all considered charge conditions a similar chemical influence of CH_4 was calculated, with deferred auto-ignition in the lean pilot-fuel mixture, and the most-reactive mixture shifts to fuel-richer conditions. Similar influence has also been observed when increasing ϕ_{CH4} in the reduced $[O_2]$ cases. Furthermore, it appears that under reduced $[O_2]$ the influence of methane is moderately amplified, visible by larger separation of curves in lean-zones.

The competing mechanism to the autoigniting flame-front is the turbulent flame propagation. It is expected to be the faster mechanism in zones with very high ignition delay stratification, e.g., in dual-fuel cases in the very lean pilot-fuel regions. To assess the influence of methane on the flame-speed, the laminar flame speed (burnt side[1]) has been calculated for a range of charge conditions (Figure 4). The calculations were performed using the same chemical mechanism as for the HR calculations [39]. At 21% $[O_2]$ (black) the highest flame speeds among the selected mixtures were predicted for around stoichiometric dodecane mixtures ranging up to 4.2 m/s. With an admixture of methane, the peak laminar flame-speed values shift to leaner pilot-fuel concentration and keep reaching similar values as for the neat air/dodecane mixture. Methane laminar flame speed at $\phi_{CH4} = 0.6$ is about 0.5 m/s. However, with a small addition of dodecane, this increases to around 1 m/s at ϕ_{C12}= 0.2 and to 4 ms at $\phi_{C12} = 0.5$. On the other hand, the laminar flame speed for lean ϕ_{C12} in the range of 0.15 – 0.5 ranges between 0.1 - 1 m/s. Not surprisingly, this indicates a considerable increase of the flame propagation speed in the leanest dodecane mixtures.

When reducing the charge oxygen content $[O_2]$ (Figure 4, blue) considerably lower flame speeds are predicted due to the reduced flame temperature and decreased reactivity. The values of ϕ relate to the fuel-concentration at 21% $[O_2]$ to enable comparison of the laminar flame speed under the same mixing state in 21% and 15% $[O_2]$ cases. Comparable flame-speeds were calculated only for the leanest conditions, where oxygen is abundant for both charges. In the fuel-richer zones, the difference becomes substantial, especially with higher ϕ_{CH4}. Combination of reduced $[O_2]$ and high ϕ_{CH4} leads to high mixture equivalence ratios and low flame speeds. The maximal flame speed is at about 1 m/s up to four times lower than in air. This indicates that the flame propagation during the transition

[1] Fresh gas laminar flame speed multiplied by the volume expansion ratio due to the change of density over the flame front

process will be considerably impaired in the reduced [O_2] cases. Therefore, the role of the ignition delay stratification will be more pronounced in these cases.

For the assessment of the transition process in spray, the influence of the flame speed increase due to the increase of charge temperature and reactivity after the first-stage ignition has been assessed in Figure 5. This has been elaborated by tracking the temporal evolution of the burnt-side laminar flame speed for selected combinations of ϕ_{CH4} and ϕ_{C12} in the air (Figure 5) analogous to Soriano and Richardson [23]. The temporal evolution of the flame speed was captured by first initiating the HR calculation. Every 10 µs the composition of the HR reactor was exported and used as the inlet flow composition of the laminar flame speed calculation. The simulation was terminated when the temperature in the HR exceeded 1050 K to avoid convergence problems due to too reactive input mixture.

During the first-stage ignition, the mixture temperature and reactivity increase, resulting in about a 20% increase of the laminar flame speed for all conditions. Thereafter, the flame speed still keeps slowly increasing as the mixture further heats up when approaching ignition. The highest change in flame speed over time is observed for conditions with highest dodecane concentration. Nevertheless, the overall temporal dependence of the flame speed is rather low. Especially in leaner mixtures, where the competition of the premixed flame propagation and autoignition is expected. Therefore, already the laminar flame-speed calculation provides a good indication of the expected flame-speed dependency on ϕ_{CH4}.

In the next sections, it was assumed for the analysis of results that the turbulent flame speed monotonously increases with the laminar-flame speed. It has to be stressed that the conclusions based on HR calculations, and laminar-flame speed represents a very simplified view of the transition process and, furthermore, used a chemical mechanism which was not validated under the experimental conditions of this study. Nevertheless, very consistent indications of the methane influence on the combustion transition governing processes have been obtained. The following sections will seek for indications of the above-observed trends.

3.2 Pilot-fuel burning traced by the CH_2O-PLIF imaging

3.2.1 Diesel cases

High-speed CH_2O-PLIF imaging enables tracing of the low-T combustion products until all pilot-fuel is consumed. Investigating the diesel-cases first, the evolution of CH_2O-PLIF signal of single events, for a variation of ET and injection pressure at T_{SOI} = 770 K, is presented in Figure 6. Due to the frame-rate limitation of the CH_2O-PLIF technique, the lowest T_{SOI} conditions have been selected for this comparison so that more relevant frames of a single event can be presented. Additionally, an EGR case (15% [O_2]) featuring similar ignition delay is presented.

The maximal pilot-fuel equivalence ratio at ignition (cp. Part 1) of these cases spans about a factor of 2 between 0.8 (ET = 300 µs) and 1.7 (ET = 500 µs). According to the 1D-flamelet simulations by Dahms et al. [38], CH_2O concentration prior to the ignition correlates well with the concentration of pilot/diesel fuel up to $\phi_{C12}\approx5$. The ET = 300 µs injection results in the leanest conditions at ignition. Before ignition, the highest PLIF signal was detected at the spray tip. However, the ignition indicated by the first CH_2O consumption has been detected in a small region around 30 mm from injector at 1.14 ms, followed by several new ignition zones at 1.24 ms aSOI. The remaining CH_2O-PLIF signal is distributed in torn-up zones with apparently lower reactivity and is rapidly consumed. Several very lean unburnt zones close to the injector persist. Such zones are believed to be too lean to autoignite and the primary source of unburnt hydrocarbons in diesel engines [44].

When the injection duration is increased (400 µs/500 µs ET, 2nd/3rd, Figure 6), higher peak CH_2O-PLIF signal was observed as expected considering the fuel-richer conditions. Following ignition, the distribution of remaining CH_2O appeared to be less distributed than in the ET = 300 µs case and limited to the jet periphery. This indicates a volumetric ignition over large zones simultaneously. Faster consumption of the residual CH_2O both at the jet periphery and close to the injector was observed when increasing ET. Due to the shorter ignition dwell time less overmixing is expected to occur near the injector, hence, reducing the very lean zones. In addition, more injection

turbulence improves the entrainment of lean mixtures into the hot burnt gases and therefore, faster lean-mixture consumption is favored.

In the high-pressure injection (1000 bar) case a more intense entrainment wave is expected after the end of injection (EOI) [45]. This is visible by the higher gradient of the CH_2O-PLIF signal from the spray tip to the injector. Differently than in the p_{inj} = 600 bar cases ignition occurs at the spray tip on the periphery of the jet and penetrates upstream and towards the spray axis. Considerable persistence of CH_2O late in the cycle implies a significant extent of lean regions upstream of the spray tip. A prolonged time for the complete pilot-fuel combustion is clearly visible also on the HRR plots (bottom plot, Figure 6).

Under the reduced [O_2] conditions the absolute fuel-concentration of the ET = 400 μs case does not change. First CH_2O is consumed at the jet periphery with a rather quick consumption of most CH_2O at the spray tip. Similar persistence of CH_2O late in the cycle was observed as in the 21% [O_2] 400 μs and 500 μs ET cases (2nd and 3rd panel, Figure 6). HRR curve shows in comparison to the 21% [O_2] case a slower HRR rise at ignition and a comparably fast drop of the HRR after the peak as in the ET = 500 μs case.

3.2.2 Dual-fuel cases

Larger variances between different pilot-injections than in diesel-cases are expected under the dual-fuel conditions due to the methane-influence on lean pilot-fuel mixtures (Figure 7). Cases with ϕ_{CH4} = 0.59 at 770 K were identified in Part 1 to exhibit a wide range of pilot-fuel combustion times (0.7 – 1.4 ms). The shorter injections have longer combustion times and were believed to be close to lean-out – the maximal ϕ_{C12} at ignition ranges between 0.4 (short injections) and 1.0 (long injection).

The evolution of CH_2O distribution during the pilot-fuel consumption in the dual-fuel cases is presented in Figure 7. In the case of short ET = 300 μs injection (1st row), ignition occurs in the zone with highest PLIF signal prior to the ignition. A slower rate of PLIF-signal disappearance is visible, and the time needed to reach the peak HRR is doubled relative to the diesel case. Surprisingly though, the persistence of CH_2O late after ignition is comparable to the diesel-case. Considering 0.55 ms longer ignition delay relative to diesel case, the pilot-fuel mixtures at ignition are much leaner. This is noteworthy since a long CH_2O persistence would be expected due to the methane influence on lean pilot zones. The flame propagation consuming the remaining CH_2O can explain these observations.

Continuing the analysis with the longer 400 and 500 μs ET injections (2nd and 3rd row, Figure 7), again ignition first occurs in the regions with the highest PLIF signal before ignition. However, particularly the 500 μs injection shows very distributed persistent CH_2O regions after the ignition. This is comparable to the ET = 300 μs injection in the diesel-case, and was not observed in the longer injection diesel cases. Considering comparable mixing state and ignition dwell time of ET = 300 μs diesel and ET = 500 μs dual-fuel case, this is not surprising. Nevertheless, in the lean zones a significantly lower persistence of CH_2O is observed at the dual-fuel case. This, again, indicates a significant role of flame propagation.

The resemblance of the high-pressure injection diesel and dual-fuel case (4th row, Figure 7) is high. Ignition occurs at the spray tip and first spreads around the periphery of the spray tip. New ignition zones then slowly consume the CH_2O upstream of the spray-head. Again, similar CH_2O persistence close to the spray tip as in the diesel-case was observed.

Contrary to the 21% [O_2] cases, a very low resemblance of the diesel and dual-fuel case has been detected in the 15% [O_2] case (5th row of Figure 7). Part 1 reported that the combination of CH_4 and reduced [O_2] leads to a reduced HRR rise and low peak-HRR. This is well visible both in the HRR and CH_2O-consumption comparison to 21% [O_2] cases. In 15% [O_2] case, a slow disappearing of CH_2O is already visible at 1.64 ms over large portions of the spray head with a large PLIF signal. This is also in-line with a small rise of HRR at that time. However, CH_2O disappears very slowly, and even in the head of the spray a considerable amount of CH_2O persists for 0.5 ms after the ignition. In the wake of the spray, CH_2O remains unburnt even longer. This is contrary to the diesel-case where no considerable

influence of reduced [O_2] on the lean CH_2O persistence was observed. Decreased flame speed (see Figure 4) combined with amplified spatial ignition-time stratification explains this observation.

3.3 Flame-contour spreading rate

Imaging of CH_2O-PLIF provides very high-fidelity images at a somewhat limited frame rate. In the diesel-cases, even at T_{SOI} = 770 K, most of the pilot-fuel was found to be consumed within 2-3 image frames (200-300 μs). This information is complemented by the line-of-sight data of the flame extent by the OH* imaging at 40 kHz frame rate. Figure 8 presents the evolution of flame-contour detected by the OH* imaging for the diesel combustion events presented in Figure 6. Nine time-instants from ignition to 0.2 ms are presented. The same plotting approach has also been repeated for the dual-fuel cases from Figure 7, presented in Figure 9.

All cases (diesel and dual-fuel at 21% [O_2], panels 1-4) show initially small ignition kernel(s) (red) which spread rapidly and merge into a larger kernel. In the diesel cases, the fast kernel spreading rate lasts for only about 100 μs after which slower spreading of contour at the spray tip and towards the injector is visible. Also, the dual-fuel cases show a fast initial kernel spreading rate, however with a lower spreading rate (contours closer together) which persist for a longer time. It takes 200-300 μs until a steady propagating contour is visible. As expected, the location and spreading rate of the OH* contours correspond well to the zones with consumed CH_2O from Figure 6 and Figure 7.

The evolution of the reduced [O_2] cases (5^{th} panel, Figure 8 and Figure 9) show somewhat "noisy" contours. At 15% [O_2] about an order of magnitude lower OH* signal relative to 21% [O_2] was experienced, resulting in a worsened signal to noise ratio. Nevertheless, a very slow spreading of the contour from the first kernel appearance up to late in the combustion cycle is visible which is in accordance to the CH_2O imaging and . Corroborating with the CH_2O-PLIF information (Figure 6 and Figure 7) it seems that CH_2O persists distributed throughout the spray tip while premixed flame propagation might have already established at the spray tip much before all pilot fuel is consumed. Therefore, the observed contour expansion might be a combined effect of pilot-fuel consumption within the jet as well as flame propagation at the edges of the contour.

To provide a more straightforward comparison, the spreading rate of flame kernels was quantified and averaged over 10 experimental repetitions. The contours from schlieren images were used since in the cases with reduced [O_2] the weak OH* signal leads to "noisy" contours. Figure 10 presents the expansion speed of the Schlieren contours for 1 ms after the autoignition for a variation of T_{SOI}, ϕ_{CH4}, [O_2] as well as injection parameters. This spreading rate was determined as the rate of change of the contour surface divided by the circumference of the contour.

At ϕ_{CH4}=0, for all cases, very high peak spreading rates in the order of 40 – 50 m/s were detected, nevertheless, persisting for only about 100 μs (Figure 10). In agreement with OH* contours (Figure 9), the peak spreading rate of the dual-fuel cases was lower at 20-30 m/s. After the peak HRR, a steady spreading rate at around 1 m/s for diesel and 3 m/s at ϕ_{CH4}=0.59 was established. In the diesel-case, this was attributed to continued air entrainment and spray penetration, while the value in the dual-fuel case correlates well to the laminar flame speed. It is worth noticing that the kernel spreading rates become comparable to the predicted laminar flame speeds already 0.3 – 0.5 ms after ignition (Figure 4).

The influence of the charge and pilot injection conditions on the spreading rate is investigated on subplots of Figure 10. First, a variation of T_{SOI} at ϕ_{CH4} = 0 and 0.59 is investigated on Figure 10a. Independent of the T_{SOI} the diesel cases show high peak spreading rate followed by a rapid drop, in agreement with the very short pilot-fuel combustion duration under these conditions. In the dual-fuel cases, a decrease in the peak spreading rate with decreasing T_{SOI} was measured. This is in agreement with the higher ignition-time gradients in leaner mixtures at ignition (Figure 3).

Extending the investigation to the variation of ET and p_{inj} Figure 10b presents the kernel spreading rate for ϕ_{CH4} = 0 and 0.59 at T_{SOI} = 810 K. No explicit dependence of the kernel expansion speed on the injection parameters is visible, neither in diesel nor in the dual-fuel case. This is also in line with very similar pilot-fuel burning times detected for this T_{SOI} (Part 1), where the conditions are believed to be far from lean-out.

Finally, the influence of reduced [O_2] content on the kernel spreading rate at T_{SOI} = 810 K was studied (Figure 10c). The influence of reduced [O_2] in the diesel case is moderate – about 35% reduction of the peak spreading rate and prolonged pilot-fuel burning was detected. At 15% [O_2] a comparable peak speed and combustion time as for T_{SOI} = 770 K (Figure 10a) was measured. This is in agreement with the higher spatial gradients of ignition-time due to the overall leaner conditions at ignition (Figure 3). On the other hand, in the dual-fuel case, the ignition delay and peak spreading rate appear to be decoupled as already observed for the pilot-fuel combustion duration in Part 1 of this work. Slow and long expansion of the kernel was observed. The ignition-time stratification due to methane in the dual-fuel cases is not sufficient to explain this observation. Only a combination of this effect with the reduced flame-speed at lower [O_2] can explain this observation.

4 Discussion

For the experimental results showing lower CH_2O persistence in dual-fuel cases, a very rapid decrease of the flame spreading rate to values comparable to the laminar flame speed is observed. In combination with a very slow burnt-zones spreading rate in the cases with reduced [O_2], a strong indication is given that, especially in the dual-fuel cases, the flame propagation is the faster combustion spreading mechanism in comparison to the auto-ignition front propagation. This effect occurs much before the complete pilot-fuel is consumed. This is an important indication for dual-fuel combustion modeling – especially in hybrid approaches coupling an auto-ignition sub-model with a flame-propagation model. In is important that the sub-model predicting higher source terms like implemented in [24] is used. Simpler approaches switching to flame propagation immediately after ignition, or approaches coupling the models based on the pilot-fuel mixture fraction, might predict non-physical solutions.

Nevertheless, another mechanism might importantly contribute to the overall combustion spreading rate: the number of ignition kernels. With an increased number of auto-ignition kernels, the generated surface for the flame-propagation mechanism is enlarged. The evolution of the OH* contours above (Figure 8 and Figure 9) shows several independent auto-ignition kernels to occur during ignition. Especially in the short injections cases (1st and 4th panels), first, several spatially separated ignition kernels are visible, which slowly merge into a single burnt zone. This considerably contributes to the overall burnt zone spreading in the initial combustion stages. Contrary, the longer injections (2nd and 3rd panels) with faster initial contour spreading show lower number of ignition kernels.

The correlation of the ignition kernels to other combustion parameters was investigated to better understand the role of ignition kernels in the transition process. The ignition kernel appearance was detected based on OH* imaging using the thresholding approach: If an area on the image exceeds the threshold, this indicates an appearance of a new kernel, except if on the preceding image at the same location a kernel has been already detected. Therefore, also the kernels formed by merging of two or more existing kernels are not counted as new. Figure 11 presents the ensemble averaged rate of new kernel appearance and cumulated kernel number for varied injection ET and p_{inj} under the dual-fuel conditions of Figure 7 and Figure 9 (T_{SOI} = 770 K, ϕ_{CH4} = 0.59).

Most of the ignition kernels for all cases in Figure 11 appear during the rapid consumption of CH_2O within the 0.2 ms after the ignition. All injections show high kernel appearance rate during this time. Due to only 10 experimental repetitions and high image frame rate, the appearance rate is noisy late after ignition. Nevertheless, a tail of the appearance rate is visible. It corresponds well to the time when new kernels appear in the wake of the spray and consume the remaining CH_2O (Figure 7 and Figure 9). The high-pressure injection with the most extended persistence of CH_2O in the wake of the jet shows most of the ignition kernels appearing late after the peak of the appearance rate. The total number of the detected ignition kernels correlates well both to the decreasing injection duration or higher p_{inj}, therefore, inversely proportional to the mean pilot-fuel equivalence ratio (ϕ_{C12}) at ignition.

This indicates that the new ignition kernels appear in rather late stages of combustion when pilot-fuel combustion is in general slow. In those cases, small fluctuations in mixture reactivity lead to new auto-ignitions. This is important since it indicates that in many cases the flame propagation is too slow to consume the very lean mixtures in the wake of the pilot-spray, and indicates a substantial role of autoignition also in the late stages of pilot-jet combustion. To

confirm this statement, Figure 12 investigates the correlations of the number of ignition kernel number to parameters relevant to fuel stratification and lean-out: ID, pilot-fuel spray volume at ignition, and pilot combustion duration (t_v).

A positive correlation of ignition kernel number to longer ignition delay, larger spray volume at ignition, and to longer pilot-fuel combustion duration is seen on Figure 12. No clear influence of methane on the number of ignition kernels is evident except for its deferring effect on ignition. Overall, these observations lead to a conclusion that conditions unfavorable for ignition lead to long ignition delays as well as slow pilot-fuel combustion, and therefore, to more distributed reactive zones and appearance of multiple ignition spots. Though the new ignition spots result in faster pilot-fuel consumption and larger initiated flame surface very low mixture reactivity appears to be needed in the first place to result in more ignition kernels. The overall low reactivity, and apparently higher stratification of the ID through the mixture, then overcompensates for the new ignition kernels. Longer ignition delay also results in a higher portion of the pilot fuel in the less reactive leaner state of mixing.

Additional confirmation of this conclusion can be gained comparing the correlation of kernel number to the ID and spray volume for different injections (Figure 12 left, middle). Shorter injections show a higher number of ignition kernels at same ID (Figure 12 left), or at same spray volume (Figure 12 middle). This clearly shows that leaner conditions at ignition lead to a larger number of ignition kernels, resulting from large lean regions upstream of the spray tip.

5 Future work

The investigations revealed a complex interplay of the methane influence of the ignition delay stratification and turbulent flame speeds. Several consistent indications of both, autoignition and turbulent mixing, playing a significant role in the transition from ignition to the premixed flame propagation clearly motivate further investigations of the topic: high-fidelity CRFD investigations in LES or DNS context could be used to elucidate the relative contributions of both kernel expansion mechanisms further, and give additional weight to the conclusions of this work. On the experimental side use of other gaseous fuels than methane could elucidate the role of premixed-fuel in the transition – by using ethane instead of methane the role of the chemical influence of methane could be highlighted. Ethane has a similar laminar flame speed but is expected to have a lower impact on the ignition delay. On the other hand, by using hydrogen instead of methane, the role of the flame-propagation can be stressed due to the increased laminar flame speed of hydrogen. Finally, with a forced ignition (laser-plasma) in the pilot-fuel plume prior to the autoignition, the turbulent flame speeds in the spray could be assessed. A comparison of the forced ignition kernel to the auto-igniting kernel expansion speed would then offer further insight into the transition process.

6 Conclusions

The underlying processes governing the pilot-fuel burning during the transition from ignition to premixed flame propagation in dual-fuel engines have been investigated in a rapid compression expansion machine. Simultaneous high-speed CH_2O-PLIF, Schlieren, and OH* chemiluminescence imaging was used to detect the pilot-fuel first-stage combustion products, ignition delay, and locations as well as the spreading rate of the ignition kernels. An extensive experimental matrix with a variation of T_{SOI}, ϕ_{CH4}, pilot injector ET, and p_{inj} as well as variation of charge oxygen content [O_2] has been acquired. Experimental investigations were corroborated with numerical calculations using homogeneous reactor and laminar flame speed simulations for different methane/dodecane/air mixtures. The investigations focused on determining the role of (a) ignition kernel number, (b) ignition delay stratification due to the chemical influence of methane and (c) the role of turbulent flame propagation on the pilot-fuel burning. Correlations of various parameters and comparison of measured values with the simulation predictions were investigated.

Based on the analysis of experimental and numerical results the following conclusions can be stated:

1. Good agreement of CH_2O formation rate (cool flames) and CH_2O consumption (high-T burning) with HRR is reported. This is further supporting the interpretation of the HRR data presented in Part 1 of this work.
2. CH_2O-PLIF imaging under lowest considered T_{SOI} indicates ignition to occur in the fuel-richest available conditions in the fuel-jet. In the cases with a long ignition dwell the fuel-jet is torn into several fuel-rich regions along the spray axes, resulting in several ignition locations. After the rapid burning of the majority of the pilot-fuel persisting CH_2O was found in the wake of the jet as well as in the very lean regions at the jet boundary.
3. HR calculations indicate considerable stratification of the lean pilot-fuel mixtures ignition delay in the mixture space. Stronger stratification was observed under reduced T_{SOI}. This explains the observed moderate prolongation of the pilot-fuel burning time t_v under the dual-fuel conditions. Also reduced $[O_2]$ conditions lead to further ID stratification. Nevertheless, this additional stratification is not sufficient to explain the additionally observed strongly prolonged pilot-fuel combustion duration under the reduced $[O_2]$ content and at comparable ID.
4. Laminar flame speed calculations predict burnt-side flame speeds of up to 6 m/s at the stoichiometric conditions. In dual-fuel mixtures, where HR calculations showed high ignition stratification ($\phi_{C12} < 0.5$), flame speeds of up to 3 m/s were predicted. With reduced $[O_2]$ at the same concentration of pilot-fuel about a factor two lower laminar flame speeds were calculated. This observation offers an explanation of the strongly prolonged pilot-fuel combustion duration in dual-fuel cases with lower $[O_2]$. If this applies, it again indicates a firm reliance of the transition process on the turbulent flame propagation through the pilot-fuel jet.
5. Maximal kernel expansion speed ranging from 35 – 50 m/s has been observed in the diesel cases while dual-fuel cases show lower peak kernel expansion speed of 20 – 30 m/s, consistently with the observed prolonged pilot combustion duration. The peak expansion speeds are considerably higher than the expected range of turbulent flame speed. However, the expansion speed quickly drops to values comparable to the laminar flame speeds of dodecane/methane/air mixtures. This gave an indication that also the turbulent flame propagation mechanism might considerably contribute to the pilot-fuel combustion before the flame propagation in the methane/air surrounding is established.
6. A strong indication of flame propagation role in the transition was given by the CH_2O persistence late after ignition. Regardless of the high ID stratification in lean mixtures (HR predictions) the diesel and dual-fuel cases showed a comparable persistence of CH_2O in the lean mixtures after 0.4 ms after ignition. This indicates that in the dual-fuel cases a considerable part of the lean pilot-fuel mixtures is burnt through the flame propagation mechanism.
7. In the initial phase of pilot-fuel burning, the flame kernels appear to spread by the mechanism of auto-igniting front spreading alongside with several new autoignition kernels appearing during the fast initial HRR. The overall number of ignition kernels increases under conditions with prolonged ID and longer dwell time. A strong correlation between the higher kernel number and longer pilot-fuel burning time was observed. This indicates that higher number of ignition kernels occurs under conditions not favorable for rapid spreading of the auto-igniting front. Methane was found to have no influence on the ignition kernel number beside it's deferring effect on the autoignition.

Overall, the findings give a detailed understanding of the involved processes of the dual-fuel combustion behavior in regard to the transition from pilot-fuel auto-ignition burning and premixed flame initiation. The comprehensive study provides essential information facilitating the further development of dual-fuel combustion modeling approaches with respect to the transition characteristics and dominant propagation mechanism. Subsequently, improved and adequate simulation methodologies can be elaborated to provide operational parameters for an optimum efficiency-emission trade-off in dual-fuel engines.

Acknowledgements:

Financial support from the Competence Center for Energy and Mobility (CCEM, project "ScheDual") and the Swiss Federal Office of Energy (grants SI/501123-01 and SI/501584-01) is gratefully acknowledged.

References:

1. Zhou, L., Liu, Y.-F., Wu, C.-B., Sun, L., et al., "Effect of the Diesel Injection Timing and the Pilot Quantity on the Combustion Characteristics and the Fine-Particle Emissions in a Micro-Diesel Pilot-Ignited Natural-Gas Engine." *Proceedings of the Institution of Mechanical Engineers, Part D: Journal of Automobile Engineering*, 2013. **227**(8): p. 1142-1152, doi: http://dx.doi.org/10.1177/0954407013480452.
2. Papagiannakis, R.G. and Hountalas, D.T., "Combustion and Exhaust Emission Characteristics of a Dual Fuel Compression Ignition Engine Operated with Pilot Diesel Fuel and Natural Gas." *Energy Conversion and Management*, 2004. **45**(18): p. 2971-2987, doi: http://dx.doi.org/10.1016/j.enconman.2004.01.013.
3. Wei, L. and Geng, P., "A Review on Natural Gas/Diesel Dual Fuel Combustion, Emissions and Performance." *Fuel Processing Technology*, 2016. **142**(Supplement C): p. 264-278, doi: http://dx.doi.org/10.1016/j.fuproc.2015.09.018.
4. Rochussen, J., Yeo, J., and Kirchen, P., "Effect of Fueling Control Parameters on Combustion and Emissions Characteristics of Diesel-Ignited Methane Dual-Fuel Combustion". 2016, SAE Technical Paper 2016-01-0792, doi: http://dx.doi.org/10.4271/2016-01-0792.
5. Liu, J., Yang, F., Wang, H., Ouyang, M., et al., "Effects of Pilot Fuel Quantity on the Emissions Characteristics of a Cng/Diesel Dual Fuel Engine with Optimized Pilot Injection Timing." *Applied Energy*, 2013. **110**(Supplement C): p. 201-206, doi: http://dx.doi.org/10.1016/j.apenergy.2013.03.024.
6. Magno, A., Mancaruso, E., and Vaglieco, B.M. "Combustion Analysis of Dual Fuel Operation in Single Cylinder Research Engine Fuelled with Methane and Diesel". 2015. SAE Technical Paper 2015-24-2461, doi: http://dx.doi.org/10.4271/2015-24-2461.
7. Papagiannakis, R.G. and Hountalas, D.T., "Experimental Investigation Concerning the Effect of Natural Gas Percentage on Performance and Emissions of a Di Dual Fuel Diesel Engine." *Applied Thermal Engineering*, 2003. **23**(3): p. 353-365, doi: http://dx.doi.org/10.1016/S1359-4311(02)00187-4.
8. Schlatter, S., Schneider, B., Wright, Y., and Boulouchos, K., "Experimental Study of Ignition and Combustion Characteristics of a Diesel Pilot Spray in a Lean Premixed Methane/Air Charge Using a Rapid Compression Expansion Machine." *SAE Technical Paper 2012-01-0825*, 2012, doi: http://dx.doi.org/10.4271/2012-01-0825.
9. Schlatter, S., Schneider, B., Wright, Y.M., and Boulouchos, K., "N-Heptane Micro Pilot Assisted Methane Combustion in a Rapid Compression Expansion Machine." *Fuel*, 2016. **179**: p. 339-352, doi: http://dx.doi.org/10.1016/j.fuel.2016.03.006.
10. Ahmad, Z., Aryal, J., Ranta, O., Kaario, O., et al., "An Optical Characterization of Dual-Fuel Combustion in a Heavy-Duty Diesel Engine." *SAE Technical Paper 2018-01-0252*, 2018, doi: http://dx.doi.org/10.4271/2018-01-0252.
11. Rochussen, J. and Kirchen, P., "Characterization of Reaction Zone Growth in an Optically Accessible Heavy-Duty Diesel/Methane Dual-Fuel Engine." *International Journal of Engine Research*, 2018: p. In press, 2019, doi: http://dx.doi.org/10.1177/1468087418756538.
12. Dronniou, N., Kashdan, J., Lecointe, B., Sauve, K., et al., "Optical Investigation of Dual-Fuel Cng/Diesel Combustion Strategies to Reduce Co $_2$ Emissions." *SAE International Journal of Engines*, 2014. **7**: p. 873-887, doi: http://dx.doi.org/10.4271/2014-01-1313.
13. Srna, A., Bruneaux, G., von Rotz, B., Bombach, R., et al., "Optical Investigation of Sooting Propensity of N-Dodecane Pilot/Lean-Premixed Methane Dual-Fuel Combustion in a Rapid Compression-Expansion Machine." *SAE Technical Paper 2018-01-0258*, 2018, doi: http://dx.doi.org/10.4271/2018-01-0258.
14. Srna, A., Bolla, M., Wright, Y.M., Herrmann, K., et al., "Effect of Methane on Pilot-Fuel Auto-Ignition in Dual-Fuel Engines." *Proceedings of the Combustion Institute*, 2018. **37**, doi: http://dx.doi.org/10.1016/j.proci.2018.06.177.
15. Srna, A., Barro, C., Herrmann, K., Möri, F., et al., "Pomdme as an Alternative Pilot Fuel for Dual-Fuel Engines: Optical Study in a Rcem and Application in an Automotive Size Dual-Fuel Diesel Engine." *SAE Technical Paper 2018-01-1734*, 2018, doi: http://dx.doi.org/10.4271/2018-01-1734.
16. Kahila, H., Wehrfritz, A., Kaario, O., and Vuorinen, V., "Large-Eddy Simulation of Dual-Fuel Ignition: Diesel Spray Injection into a Lean Methane-Air Mixture." *Combustion and Flame*, 2019. **199**: p. 131-151, doi: http://dx.doi.org/10.1016/j.combustflame.2018.10.014.
17. Abd Alla, G.H., Soliman, H.A., Badr, O.A., and Abd Rabbo, M.F., "Effect of Pilot Fuel Quantity on the Performance of a Dual Fuel Engine." *Energy Conversion and Management*, 2000. **41**(6): p. 559-572, doi: http://dx.doi.org/10.1016/S0196-8904(99)00124-7.

18. Abdelaal, M.M. and Hegab, A.H., "Combustion and Emission Characteristics of a Natural Gas-Fueled Diesel Engine with Egr." *Energy Conversion and Management*, 2012. **64**: p. 301-312, doi: http://dx.doi.org/10.1016/j.enconman.2012.05.021.
19. Nithyanandan, K., Gao, Y., Wu, H., Lee, C.-F., et al., "An Optical Investigation of Multiple Diesel Injections in Cng/Diesel Dual-Fuel Combustion in a Light Duty Optical Diesel Engine". 2017, SAE Technical Paper 2017-01-0755, doi: http://dx.doi.org/10.4271/2017-01-0755.
20. Barro, C., Nani, C., Hutter, R., and Boulouchos, K., "Spray Model Based Phenomenological Combustion Description and Experimental Validation for a Dual Fuel Engine". 2017, SAE International, doi: http://dx.doi.org/10.4271/2017-24-0098.
21. Papagiannakis, R.G. and Hountalas, D.T., "Combustion and Exhaust Emission Characteristics of a Dual Fuel Compression Ignition Engine Operated with Pilot Diesel Fuel and Natural Gas." *Energy Conversion and Management*, 2004. **45**(18-19): p. 2971-2987, doi: http://dx.doi.org/10.1016/j.enconman.2004.01.013.
22. Wissink, M.L., Curran, S.J., Roberts, G., Musculus, M.P.B., et al., "Isolating the Effects of Reactivity Stratification in Reactivity-Controlled Compression Ignition with Iso-Octane and <I>N</I> -Heptane on a Light-Duty Multi-Cylinder Engine." *International Journal of Engine Research*, 2017: p. 146808741773289, doi: http://dx.doi.org/10.1177/1468087417732898.
23. Soriano, B.S. and Richardson, E.S., "Investigation of Flame Propagation in Autoignitive Blends of N-Heptane and Methane Fuel." *Combustion Science and Technology*. **Under Review**.
24. Soriano, B.S., Richardson, E.S., Schlatter, S., and Wright, Y.M., "Conditional Moment Closure Modelling for Dual-Fuel Combustion Engines with Pilot-Assisted Compression Ignition." *SAE Technical Paper 2017-01-2188*, 2017, doi: http://dx.doi.org/10.4271/2017-01-2188.
25. Goyal, H., Kook, S., and Ikeda, Y., "The Influence of Fuel Ignition Quality and First Injection Proportion on Gasoline Compression Ignition (Gci) Combustion in a Small-Bore Engine." *Fuel*, 2019. **235**: p. 1207-1215, doi: http://dx.doi.org/10.1016/j.fuel.2018.08.090.
26. Vallinayagam, R., An, Y., S.Vedharaj, Sim, J., et al., "Naphtha Vs. Dieseline – the Effect of Fuel Properties on Combustion Homogeneity in Transition from Ci Combustion Towards Hcci." *Fuel*, 2018. **224**: p. 451-460, doi: http://dx.doi.org/10.1016/j.fuel.2018.03.123.
27. Kokjohn, S.L., Musculus, M.P.B., and Reitz, R.D., "Evaluating Temperature and Fuel Stratification for Heat-Release Rate Control in a Reactivity-Controlled Compression-Ignition Engine Using Optical Diagnostics and Chemical Kinetics Modeling." *Combustion and Flame*, 2015. **162**(6): p. 2729-2742, doi: http://dx.doi.org/10.1016/j.combustflame.2015.04.009.
28. Bakker, P.C., Maes, N., and Dam, N., "The Potential of on- and Off-Resonant Formaldehyde Imaging Combined with Bootstrapping in Diesel Sprays." *Combustion and Flame*, 2017. **182**: p. 20-27, doi: http://dx.doi.org/10.1016/j.combustflame.2017.03.032.
29. Skeen, S.A., Manin, J., and Pickett, L.M., "Simultaneous Formaldehyde Plif and High-Speed Schlieren Imaging for Ignition Visualization in High-Pressure Spray Flames." *Proceedings of the Combustion Institute*, 2015. **35**: p. 3167-3174, doi: http://dx.doi.org/10.1016/j.proci.2014.06.040.
30. Lachaux, T. and Musculus, M.P.B., "In-Cylinder Unburned Hydrocarbon Visualization During Low-Temperature Compression-Ignition Engine Combustion Using Formaldehyde Plif." *Proceedings of the Combustion Institute*, 2007. **31**: p. 2921-2929, doi: http://dx.doi.org/10.1016/j.proci.2006.07.044.
31. Srna, A., Bruneaux, G., von Rotz, B., Bombach, R., et al., "Optical Investigation of Sooting Propensity of N-Dodecane Pilot/Lean-Premixed Methane Dual-Fuel Combustion in a Rapid Compression-Expansion Machine". 2018, SAE Technical Paper 2018-01-0258, doi: http://dx.doi.org/10.4271/2018-01-0258.
32. O'Connor, J. and Musculus, M., "Optical Investigation of the Reduction of Unburned Hydrocarbons Using Close-Coupled Post Injections at Ltc Conditions in a Heavy-Duty Diesel Engine." *SAE International Journal of Engines*, 2013. **6**(1): p. 379-399, doi: http://dx.doi.org/10.4271/2013-01-0910.
33. Collin, R., Nygren, J., Richter, M., Aldén, M., et al., "Simultaneous Oh-and Formaldehyde-Lif Measurements in an Hcci Engine." *SAE Technical paper 2003-01-3218*, 2003, doi: http://dx.doi.org/10.4271/2003-01-3218.
34. Skeen, S., Manin, J., and Pickett, L.M., "Visualization of Ignition Processes in High-Pressure Sprays with Multiple Injections of N-Dodecane." *SAE International Journal of Engines*, 2015. **8**: p. 696-715, doi: http://dx.doi.org/10.4271/2015-01-0799.
35. Salaun, E., Apeloig, J., Grisch, F., Yvonnet, C.-E., et al. "Optical Investigation of Ignition Timing and Equivalence Ratio in Dual-Fuel Cng/Diesel Combustion". 2016. SAE Technical Paper 2016-01-0772, doi: http://dx.doi.org/10.4271/2016-01-0772.

36. Najafabadi, M.I., Egelmeers, L., Somers, B., Deen, N., et al., "The Influence of Charge Stratification on the Spectral Signature of Partially Premixed Combustion in a Light-Duty Optical Engine." *Applied Physics B*, 2017. **123**, doi: http://dx.doi.org/10.1007/s00340-017-6688-9.
37. Pickett, L.M., "Engine Combustion Network." *http://www.sandia.gov/ecn/dieselSprayCombustion.php*, 2013.
38. Dahms, R.N., Paczko, G.n.A., Skeen, S.A., and Pickett, L.M., "Understanding the Ignition Mechanism of High-Pressure Spray Flames." *Proceedings of the Combustion Institute*, 2017. **36**: p. 2615-2623, doi: http://dx.doi.org/10.1016/j.proci.2016.08.023.
39. RANZI, E., FRASSOLDATI, A., STAGNI, A., PELUCCHI, M., et al., "Reduced Kinetic Schemes of Complex Reaction Systems: Fossil and Biomass - Derived Transportation Fuels." *International Journal of Chemical Kinetics*, 2014. **46**(9): p. 512-542, doi: http://dx.doi.org/doi:10.1002/kin.20867.
40. Ghaderi Masouleh, M., Wehrfritz, A., Kaario, O., Kahila, H., et al., "Comparative Study on Chemical Kinetic Schemes for Dual-Fuel Combustion of N-Dodecane/Methane Blends." *Fuel*, 2017. **191**: p. 62-76, doi: http://dx.doi.org/10.1016/j.fuel.2016.10.114.
41. Ranzi, E., Frassoldati, A., Grana, R., Cuoci, A., et al., "Hierarchical and Comparative Kinetic Modeling of Laminar Flame Speeds of Hydrocarbon and Oxygenated Fuels." *Progress in Energy and Combustion Science*, 2012. **38**(4): p. 468-501, doi: http://dx.doi.org/10.1016/j.pecs.2012.03.004.
42. Sarathy, S.M., Westbrook, C.K., Mehl, M., Pitz, W.J., et al., "Comprehensive Chemical Kinetic Modeling of the Oxidation of 2-Methylalkanes from C7 to C20." *Combustion and Flame*, 2011. **158**: p. 2338-2357, doi: http://dx.doi.org/10.1016/j.combustflame.2011.05.007.
43. Zeldovich, Y.B., "Regime Classification of an Exothermic Reaction with Nonuniform Initial Conditions." *Combustion and Flame*, 1980. **39**(2): p. 211-214, doi: http://dx.doi.org/10.1016/0010-2180(80)90017-6.
44. Musculus, M.P., Lachaux, T., Pickett, L.M., and Idicheria, C.A., "End-of-Injection over-Mixing and Unburned Hydrocarbon Emissions in Low-Temperature-Combustion Diesel Engines." *SAE Technical Paper 2007-01-0907*, 2007, doi: http://dx.doi.org/10.4271/2007-01-0907.
45. Musculus, M.P. and Kattke, K., "Entrainment Waves in Diesel Jets." *SAE International Journal of Engines*, 2009. **2**: p. 1170–1193, doi: http://dx.doi.org/10.4271/2009-01-1355.

Abbreviations

$[O_2]$	Charge oxygen concentration [vol %]
BDC	Bottom Dead Center
CFD	Computational Fluid Dynamics
EGR	Exhaust Gas Recirculation
EOI	End of Injection
ET	injector Energizing Time
ϕ	Equivalence ratio
ϕ_{C12}	Dodecane in air equivalence ratio
ϕ_{CH4}	Charge methane equivalence ratio
FHWM	Full-Width at Half-Maximum
HR	Homogeneous Reactor
HRR	Heat Release Rate
ID	Ignition Delay
NO_x	Nitrogen oxides
OH*	Chemically excited hydroxyl radical
PAH	Poly-Aromatic Hydrocarbons
p_{inj}	Injection pressure
PLIF	Planar Laser-Induced Fluorescence
RCEM	Rapid Compression-Expansion Machine
SOI	hydraulic Start of Injection
TDC	Top Dead Center
T_{SOI}	Charge temperature at SOI
t_v	Pilot-fuel combustion duration metric
UHC	Unburnt HydroCarbons
UV	Ultra-Violet

Figures:

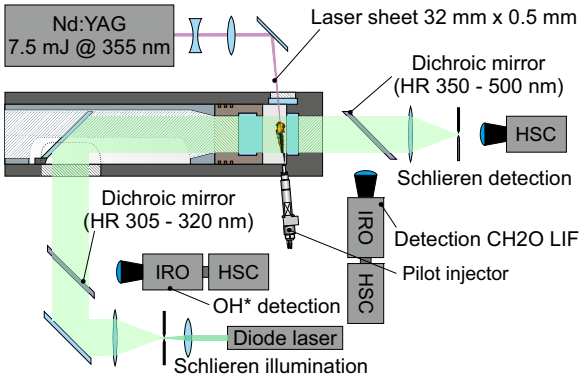

Figure 1: Optical setup for simultaneous high-speed Schlieren, CH_2O-PLIF and OH* chemiluminescence imaging at RCEM [14].

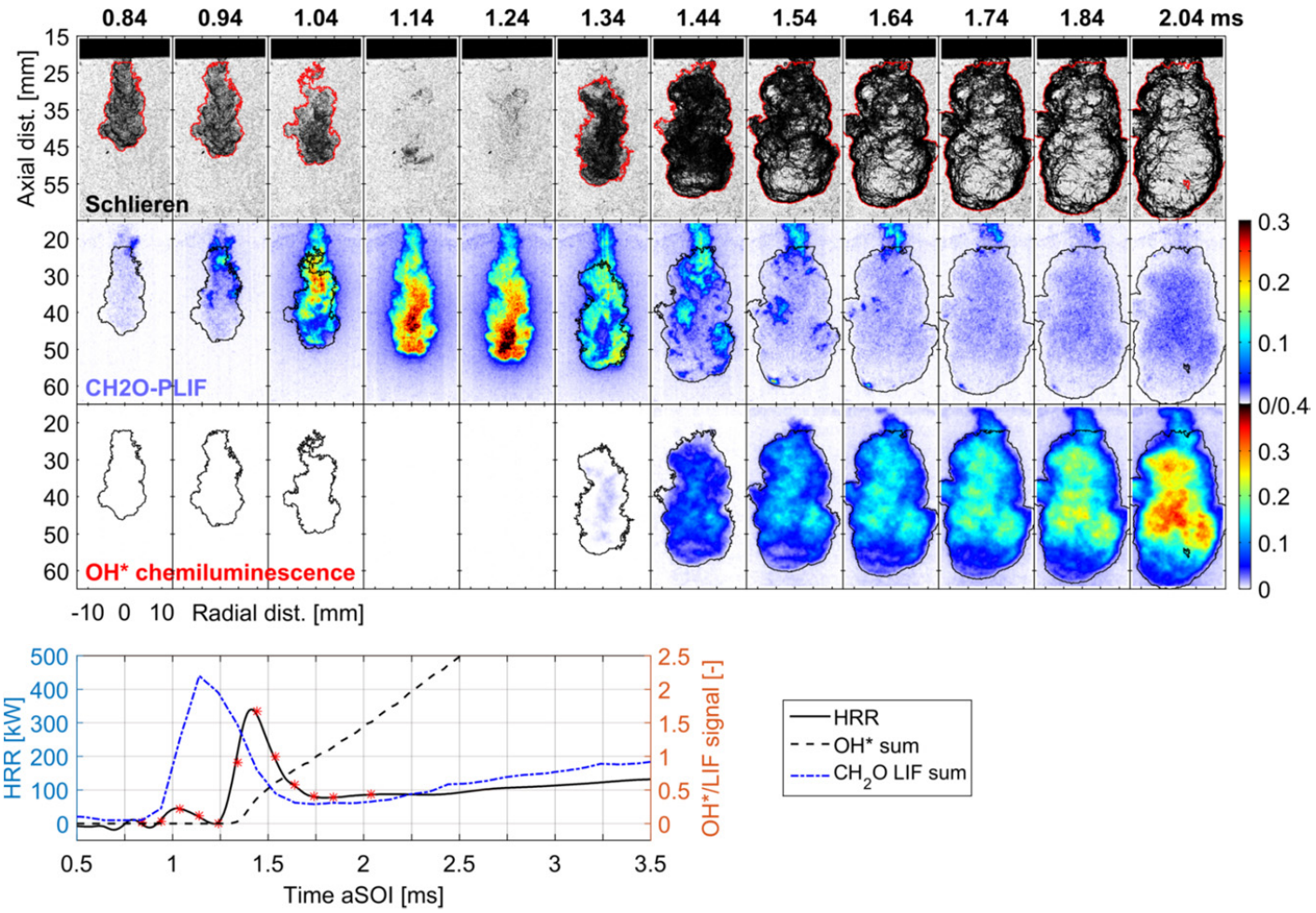

Figure 2: A series of image panels showing the simultaneously acquired raw images from Schlieren (upper row), CH_2O-PLIF (middle row) and OH* chemiluminescence (bottom row). Overlaid are the spray contours from processed Schlieren images. Time aSOI is indicated above each column. The bottom plot shows the HRR, total OH* chemiluminescence signal, and total CH_2O-PLIF signal. Asterisk symbols indicate the time instants of the image-panels above. Conditions: T_{SOI} = 810 K, ϕ_{CH4} = 0.59, ET = 400 µs, p_{inj} = 600 bar.

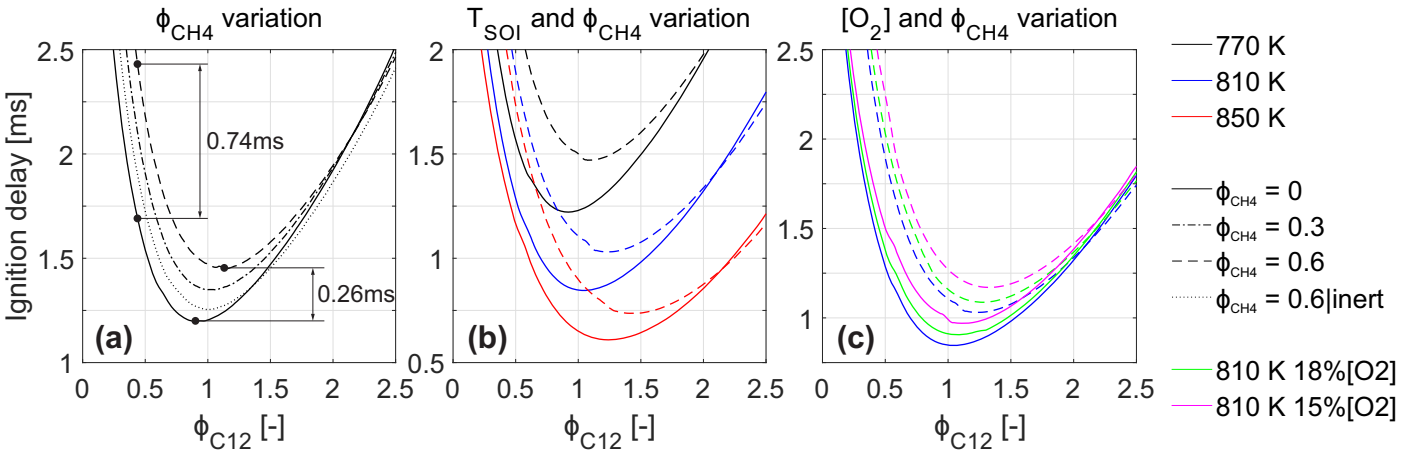

Figure 3: Homogeneous reactor simulations of the ignition delay dependence on pilot-fuel equivalence ratio for (a) a variation of ϕ_{CH4} at a fixed T_{SOI} = 770 K, (b) variation of T_{SOI} and ϕ_{CH4}, and (c) variation of [O_2] and ϕ_{CH4}. Line color determines the T_{SOI} and [O_2], line-style the ϕ_{CH4}. The dotted line (a) shows the ignition delay dependence when methane has been added to the chemical mechanism as an inert species. The ϕ_{C12} describes the equivalence ratio of dodecane related to 21% [O_2], also in the EGR cases (c).

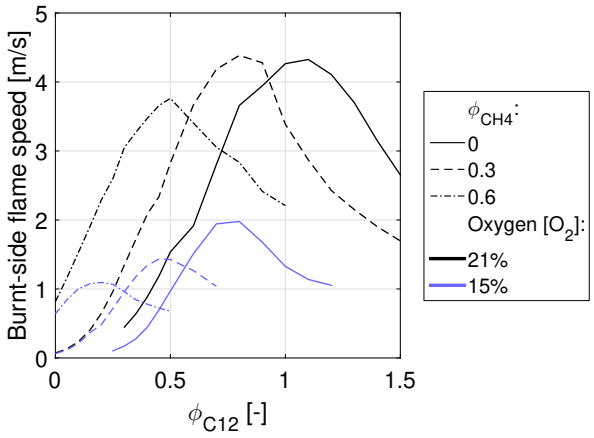

Figure 4: Burnt-side laminar flame speed dependence on ϕ_{C12} for a variation of ϕ_{CH4} (line style) and [O_2] (color), T_{SOI} = 850 K.

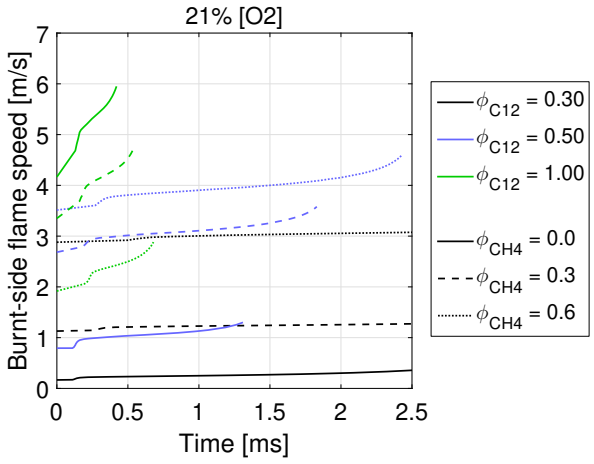

Figure 5: Temporal evolution of burnt-side flame speed in mixtures of CH_4 and dodecane at 850 K and 21% [O_2]. Line color determines the ϕ_{C12}, line-style the ϕ_{CH4}. The lines are drawn up to the time shortly before ignition.

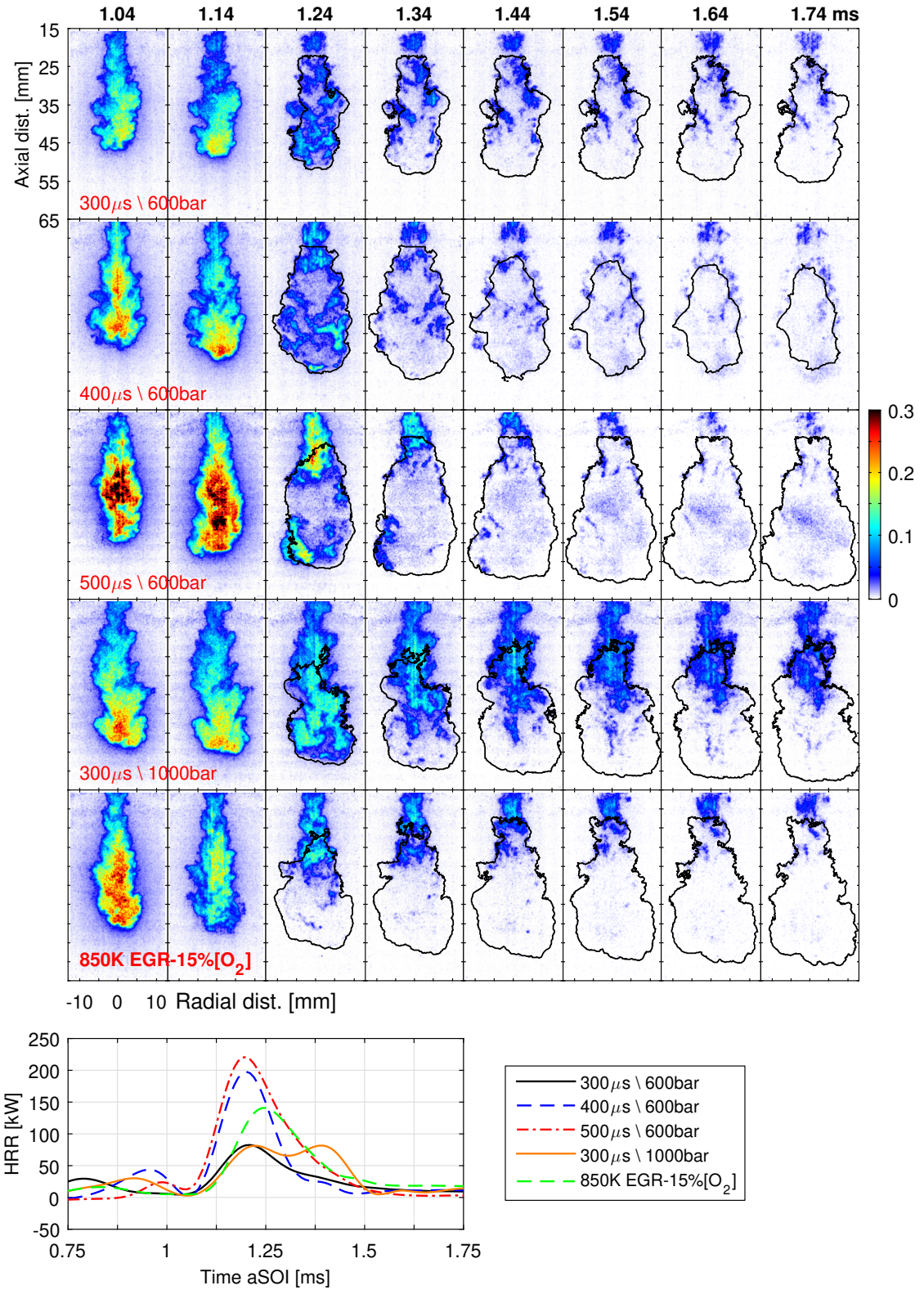

Figure 6: Diesel-case CH_2O-PLIF image time-series for variations of pilot injection parameters: ET variation (rows 1-3), p_{inj} variation (row 4) and $[O_2]$ variation (row 5, ET = 400 µs, p_{inj} = 600 bar). Simultaneously acquired Schlieren contours are superimposed on panels after the ID (black line). The bottom plot shows the HRR for all five cases. T_{SOI} = 770 K (except 15% $[O_2]$ case, row 5).

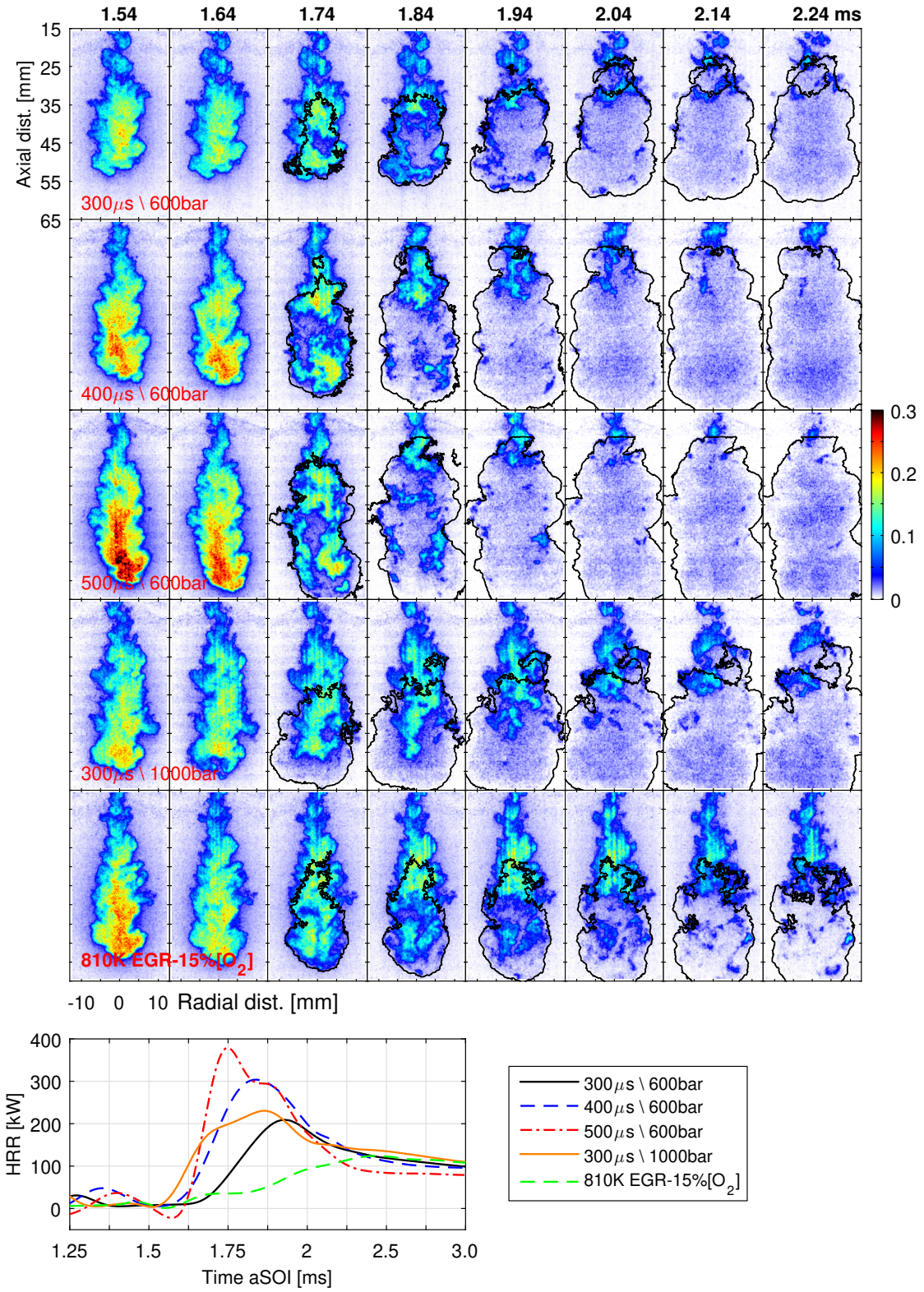

Figure 7: Dual-fuel (ϕ_{CH4} = 0.59) cases CH_2O-PLIF image time-series for variations of pilot injection parameters: ET variation (rows 1-3), p_{inj} variation (row 4) and $[O_2]$ variation (row 5, ET = 400 μs, p_{inj} = 600 bar). Simultaneously acquired Schlieren contours are superimposed on panels after the ID (black line). The bottom plot shows the HRR for all five cases. T_{SOI} = 770 K (except 15% $[O_2]$ case, row 5).

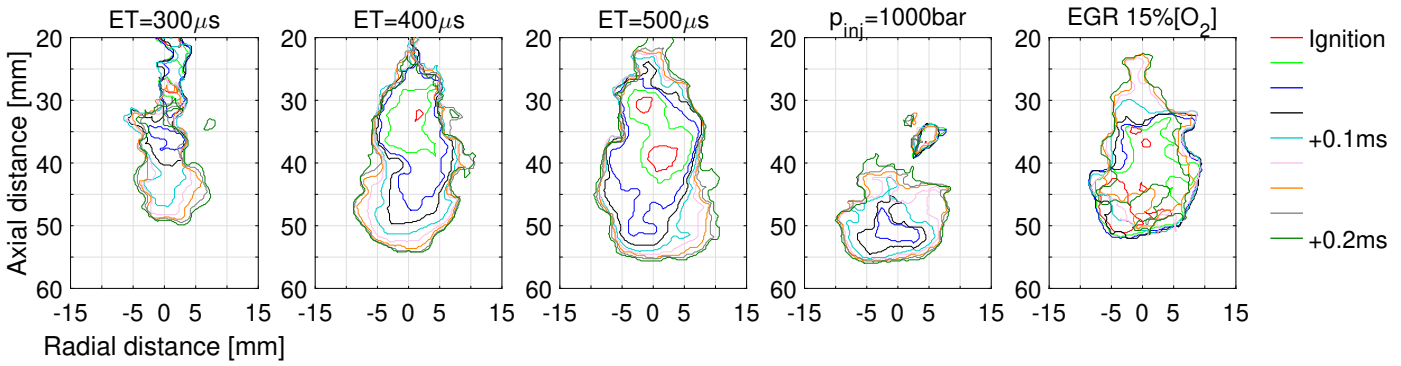

Figure 8: Diesel case single-shot evolution of OH* imaging based burnt zone contour. The time separation between contours is 25 μs. T_{SOI} = 770 K. The same combustion events as in Figure 6 are presented.

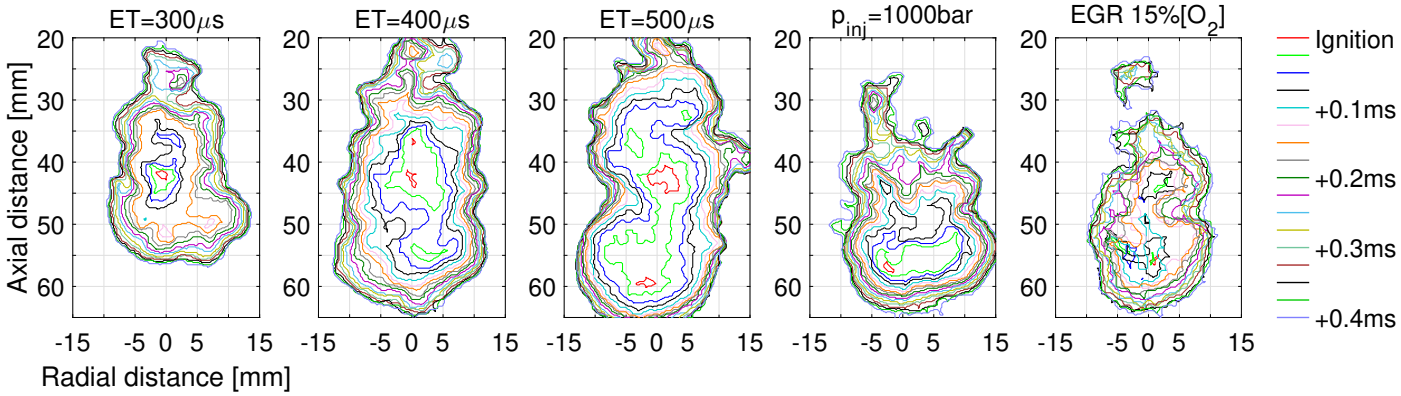

Figure 9: Dual-fuel case (ϕ_{CH4} = 0.59) single-shot evolution of OH* imaging, based burnt zone contour. The time separation between contours is 25 μs. T_{SOI} = 770 K. The same combustion events as in Figure 7 are presented.

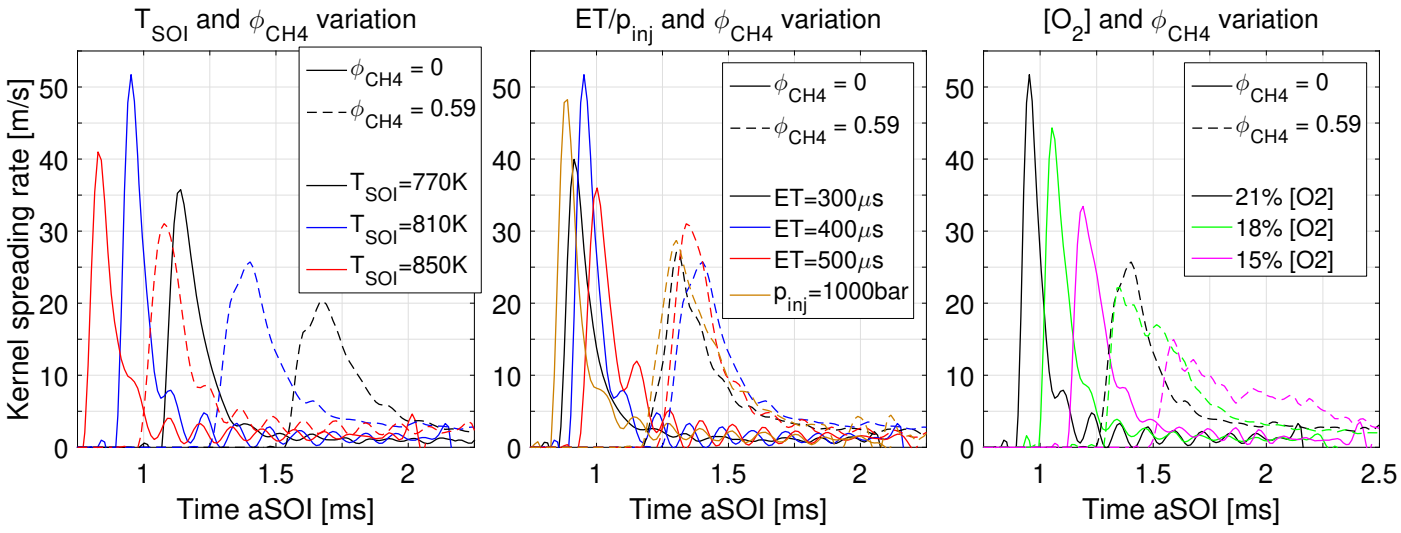

Figure 10: Schlieren-based evolution of the kernel spreading-rate: (a) ϕ_{CH4} and T_{SOI} variation, (b) Injection $\phi_{CH4,}$ and ET or p_{inj} variation at T_{SOI} = 810 K and (c) ϕ_{CH4} and [O_2] variation.

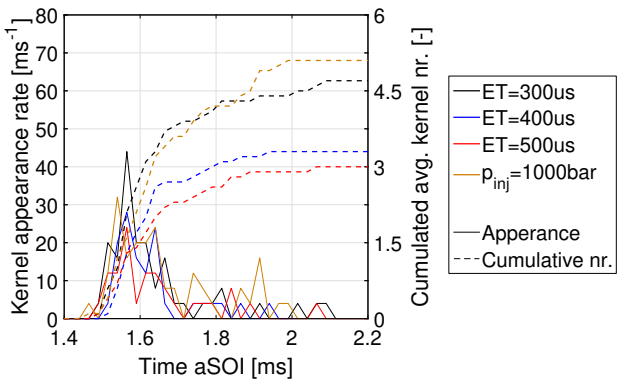

Figure 11: OH* based ensemble-averaged ignition kernel appearance rate and ensemble-averaged cumulated ignition kernels number for a variation of ET and p_{inj}. Conditions: T_{SOI} = 770 K, ϕ_{CH4} = 0.59.

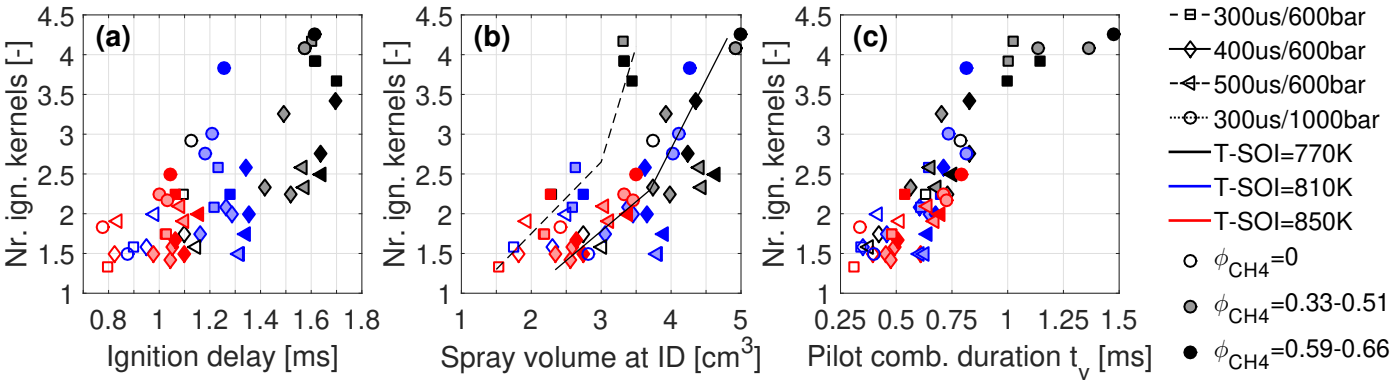

Figure 12: (a) Correlation of ignition kernel number to the ignition delay, (b) to the spray volume at ignition, and (c) to the pilot-fuel combustion duration t_v (right). Marker shape indicates the pilot injection parameters, marker color the T_{SOI} and marker fill the ϕ_{CH4}, according to the legend. The added lines shall help the reader to orient on the plot.